Large unsaturated transverse and negative longitudinal magnetoresistance in the compensated semimetal $MoGe_2$

Yi-Fei Huang,[1,2,*] Wen-Liang Zhu,[1,2,*] Yi-Yan Wang,[1] Qing-Xin Dong,[1,2] Li-Bo Zhang,[1,2] Chen-Sheng Li,[1,2] Hao OuYang,[1,2] Zhi-An Ren,[1,2,3] and Gen-Fu Chen[1,2,3,†]

[1]*Institute of Physics and Beijing National Laboratory for Condensed Matter Physics, Chinese Academy of Sciences, Beijing 100190, China*
[2]*School of Physical Sciences, University of Chinese Academy of Sciences, Beijing 100049, China*
[3]*Songshan Lake Materials Laboratory, Dongguan, Guangdong 523808, China*

(Received 1 February 2021; accepted 12 April 2021; published 21 April 2021)

We report the experimental results of magnetotransport on the single crystal $MoGe_2$, which was theoretically predicated to be a topological insulator. The resistivity of $MoGe_2$ exhibits a metallic behavior at zero field, while with magnetic fields applied along the z axis and perpendicular to current, $MoGe_2$ presents an upturn resistivity behavior and unsaturated quadratic large magnetoresistance (MR). The analysis of Hall effect shows that $MoGe_2$ is a compensated semimetal with high mobilities at low temperatures, which is the origin of resistivity upturn and unsaturated large MR. As magnetic fields parallel to current, $MoGe_2$ shows a weak antilocalization effect at low fields and a pronounced negative MR at higher fields, which is analogous to the picture of the Adler-Bell-Jackiw axial anomaly. Our results indicate that $MoGe_2$ is a topological semimetal rather than a topological insulator, and will encourage further theoretical and experimental investigations on this compound.

DOI: 10.1103/PhysRevB.103.134116

I. INTRODUCTION

The discovery of topological insulators (TIs) [1–4] sparked intense research interests in condensed matter physics and material science, because of the nontrivial band structures characterized by insulating bulk states and two-dimensional gapless surface states. Moreover, the realization of new topological states in the materials other than insulators, such as topological semimetals (TSMs) [5–7], which host a linear dispersion at the crossing of the valence and conduction bands near the Fermi energy, has become one of the most fascinating and challenging topics. According to the degeneracy and dimensionality of the nodal points near the Fermi energy, TSMs can be classified into several categories, such as Dirac semimetals [8–11], Weyl semimetals [12–15], and nodal-line semimetals [16,17], as well as those from threefold (or higher) band degeneracies [18,19]. These nontrivial topological-protected band structures usually can allow topological materials to present novel physical properties and potential applications.

Recently, molybdenum binary compounds (MBCs) MoX_2, such as $MoTe_2$ and $MoSi_2$, have attracted substantial attention because of the discovery of novel quantum phenomena [20–24]. For instance, Weyl semimetal $MoTe_2$ exhibits a bulk superconductivity with $T_c \sim 0.1$ K [25] and a nontrivial surface superconductivity state [26]. These results may introduce a new pathway for the exploration of topological superconductivity. In addition, $MoSi_2$ displays a unsaturated large magnetoresistance (LMR) driven by Zeeman effect at high magnetic fields, which is different from that caused by the electron-hole compensation in the reported work [22]. Although the underlying physics of intriguing features in these materials is still not confirmed completely, these reported MBCs provide the platform for the investigation of exotic physical properties. Therefore, more MBCs are strongly desired to search for new physics and realize potential application.

Currently, $MoGe_2$, crystallizing in an orthorhombic structure with *Pnma* space group, has been predicted to be a new candidate of TIs [27,28], which is expected to host novel phenomena and shed more light on the physical properties observed in MBCs. However, the previous research on $MoGe_2$ was very limited, only focusing on the crystallographic and thermal characterization [29–32]. In this paper, we have successfully grown single crystal $MoGe_2$ and performed the systematic magnetotransport studies with the temperatures ranging from 2.5 K to 300 K at magnetic fields up to 9 T. We observed a large transverse positive $\mathrm{MR}(B) = [\rho_{xx}(B) - \rho_{xx}(0)] \times 100\%/\rho_{xx}(0)$, which exhibits a unsaturated quadratic behavior. The analysis of MR and Hall resistivity with semiclassical two-band model reveals that the balance between holes and electrons and high mobilities in the $MoGe_2$ could be responsible for the unsaturated quadratic LMR at high magnetic fields. Remarkably, a weak antilocalization (WAL) effect arises with the rotation of magnetic field in the xz plane, and a pronounced negative magnetoresistance (NMR) can only be observed when applied magnetic fields are parallel to current, which is analogous to the picture of the Adler-Bell-Jackiw (ABJ) chiral anomaly of Weyl nodes [12,33–38] splitting from surface Dirac points at a certain direction. These findings suggest that a strong signature of three-dimensional (3D) Dirac or Weyl fermions' characters

*These authors contributed equally to this work.
†gfchen@iphy.ac.cn

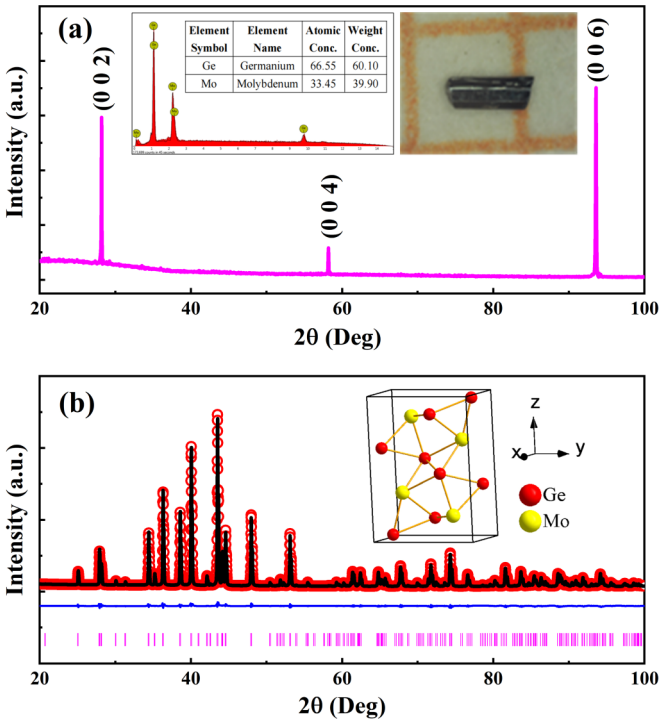

FIG. 1. (a) Single crystal XRD pattern of $MoGe_2$. The left inset is the EDX spectroscopy of $MoGe_2$. The right inset is typical image of single crystal $MoGe_2$ with strip shape. (b) Powder XRD pattern of $MoGe_2$ with refinement. Red circle and black solid line show the data of experiment and the fitting curve, respectively. The difference plot is in blue. The pink lines denote the positions of Bragg peaks of $MoGe_2$. The inset shows crystal structure of $MoGe_2$, in which red and yellow balls represent Ge and Mo, respectively.

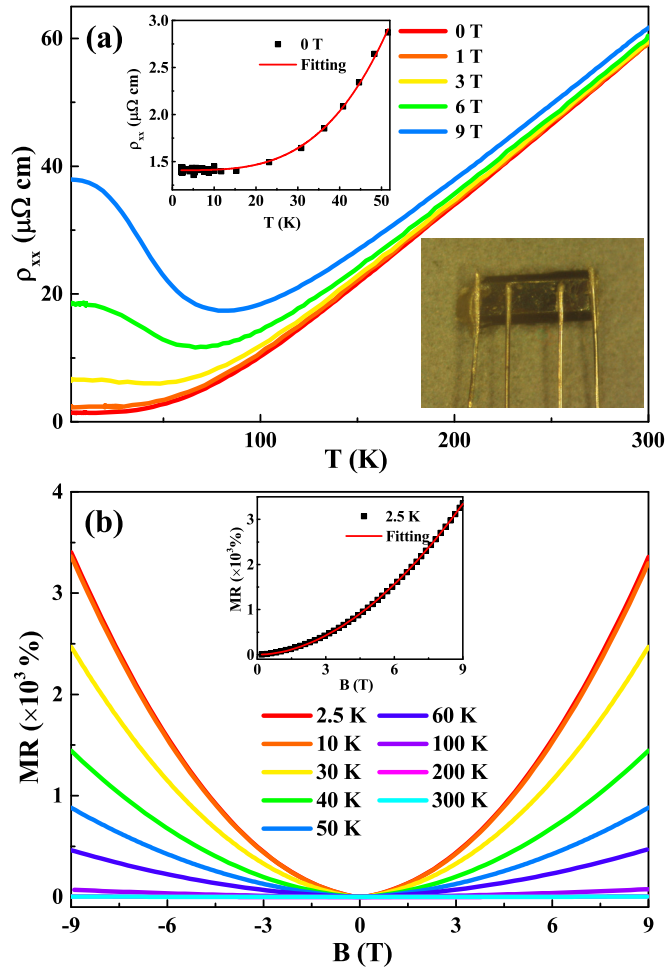

FIG. 2. Magnetotransport property of $MoGe_2$. (a) Temperature dependence of resistivity ρ for magnetic fields perpendicular to current under different magnetic fields. The upper inset shows the fitting resistivity at zero field using the formula $\rho = \rho_0 + AT^n$. The lower inset shows an optical image of the standard four-probe transport measurements on the single crystal $MoGe_2$. (b) Magnetic field dependence of MR for magnetic fields perpendicular to current at different temperatures. The inset shows the fitting result of zero-field resistivity with the formula $MR = aB^n$ at 2.5 K.

exists in the $MoGe_2$ as detected in other TSMs [12,34,36], although first-principles calculations indicate that $MoGe_2$ is a TI. Our work will stimulate further theoretical and experimental investigations on the nontrivial band topology in the $MoGe_2$.

II. EXPERIMENTAL METHODS AND CRYSTAL STRUCTURE

Single crystals of $MoGe_2$ were grown from Ge fluxes. The mixture of Mo and Ge was placed into an alumina crucible with a molar ratio of 1:30 and sealed in a quartz tube. The quartz tube was heated to 1150 °C, held for 20 h, and then slowly cooled to 1000 °C at a rate of 1 °C/h. Finally, the excess Ge flux was removed with a centrifuge. The obtained single crystals are of strip shape with about 1 mm length, as shown in the right inset of Fig. 1(a). The average Mo:Ge atomic ratio determined using the energy dispersive x-ray (EDX) spectroscopy is very close to 1:2 and no foreign elements were detected within the limitation of instrument resolution, as shown in the left inset of Fig. 1(a). The crystal structure was characterized by x-ray diffraction (XRD) using a PANalytical Diffractometer with Cu K_α radiation at room temperature. Electrical transport measurements were carried out by a Quantum Design PPMS-9 T.

$MoGe_2$ crystallizes in an orthorhombic structure [inset of Fig. 1(b)] with a space group *Pnma* (No. 62). Figure 1(a) shows the single crystal XRD pattern of a sample. All of the peaks can be identified as the (0 0 l) reflections of $MoGe_2$. Figure 1(b) shows the room-temperature powder XRD pattern of the obtained $MoGe_2$, in which all the powder diffraction peaks can be well indexed in the *Pnma* space group. The determined lattice parameters $a = 6.344$ Å, $b = 3.450$ Å, and $c = 8.586$ Å are in good agreement with the previously reported data [29].

III. RESULTS AND DISCUSSION

The temperature-dependent dc resistivity of $MoGe_2$ under selected magnetic fields with B parallel to z axis and perpendicular to current ($I = 1$ mA) is shown in Fig. 2(a). The lower inset of Fig. 2(a) shows the photograph of a transport-

measurement single crystal $MoGe_2$ with the dimensions of $0.71 \times 0.18 \times 0.14\,mm^3$, in which four Pt wires were adhered to the sample with the silver paste. At zero field, the resistivity presents a metallic behavior with a residual-resistivity-ratio ($RRR = R_{300\,K}/R_{2.5\,K}$) up to 40. The upper inset of Fig. 2(a) shows a simulation of the zero-field resistivity from 2.5 K to 50 K with the formula $\rho = \rho_0 + AT^n$, where $\rho_0 = 1.4\,\mu\Omega\,cm$, $A = 2.1 \times 10^{-6}\ \mu\Omega\,cm\,K^{-3.4}$, and $n = 3.4$. The value of n is neither 2 for electron-electron scattering nor 5 for conventional electron-phonon scattering by the Bloch-Grüneisen theory [39], almost close to that in LaBi and $ZrSb_2$ [40,41], in which the interband electron-phonon scattering was considered to result in the temperature-dependent resistivity at low temperatures. With the application of magnetic fields, the metallic behavior is weakening and a definite upturn is observed at low temperatures, as shown in Fig. 2(a). The upturn resistivity behavior can be enhanced with increasing magnetic fields, which has been observed in many compensated semimetals, including recently discovered compounds like $NbAs_2$ and WC [19,42,43]. Figure 2(b) shows the magnetic field-dependent MR at different temperatures with B along z axis and perpendicular to current, where the MR increases with increasing magnetic fields and decreasing temperatures. Until 2.5 K and 9 T, the MR reaches to the maximum 3400% and has no any sign of saturation. The fitting curve for MR at T = 2.5 K by the expression $MR = aB^n$ is shown in the inset of Fig. 2(b), in which the obtained index $n = 1.87$, close to 2. The deviation from the quadratic behavior implies that there may be a slight imbalance between electrons and holes in the $MoGe_2$. The resistivity upturn and unsaturated quadratic LMR at low temperatures can be attributed to the balance between electrons and holes and high mobilities [40,44,45]. According to the semiclassical two-band model [39,40,44], the resistivity with multiband system under magnetic fields can be described as

$$\rho_{xx}(B) = \frac{1}{e}\frac{(n_h\mu_h + n_e\mu_e) + (n_e\mu_h + n_h\mu_e)\mu_h\mu_e B^2}{(n_h\mu_h + n_e\mu_e)^2 + (n_e - n_h)^2(\mu_h\mu_e)^2B^2}, \quad (1)$$

then the MR is

$$\mathrm{MR}(B) = \frac{n_e\mu_e n_h\mu_h(\mu_h + \mu_e)^2B^2}{(n_h\mu_h + n_e\mu_e)^2 + (n_e - n_h)^2(\mu_h\mu_e)^2B^2}. \quad (2)$$

If the electron density and hole density keep balance ($n_c = n_e = n_h$), the MR presents a quadratic dependence on the magnetic fields, $\mathrm{MR}(B) = \mu_h\mu_e B^2$, which indicates that the compensation of electrons and holes densities and high mobilities are related to unsaturated quadratic LMR. Moreover, based on the Kohler's rule [39,44], $\mathrm{MR}(B) = \alpha(B/\rho_{xx}(T,0))^m$, in which $m = 2$. Considering $\rho_{xx}(T,0) = \rho_0 + AT^n$, we can obtain

$$\rho_{xx}(T,B) = \rho_0 + AT^n + \alpha B^2/(\rho_0 + AT^n), \quad (3)$$

where $\alpha = \kappa[n_c e(1+\kappa)]^{-2}$ and $\kappa = \mu_h/\mu_e$ [44]. It is apparent that there is a minimum in the ρ_{xx} curve, resulting in the resistivity upturn. Therefore, the resistivity upturn and unsaturated quadratic LMR at low temperatures can originate from the compensation of electrons and holes densities and high mobilities.

To shed more light on the mechanism of unsaturated quadratic LMR and the upturn resistivity behavior, we have performed a Hall-effect measurement on the single crystal of $MoGe_2$ at various temperatures with magnetic fields along the z axis. Figures 3(a) and 3(b) show the field-dependent Hall resistivity ρ_{xy} and longitudinal conductivity σ_{xx} [$\sigma_{xx} = \rho_{xx}/({\rho_{xx}}^2 + {\rho_{xy}}^2)$] at temperatures ranging from 2.5 K to 300 K. At low temperatures, the negative slope of ρ_{xy} suggests that electron-type carriers dominate the transport process. While at higher temperatures, ρ_{xy} has a negative slope at low fields and a positive slope at high fields, which shows the coexistence of hole-type and electron-type carriers in the $MoGe_2$. The nonlinear field dependence of ρ_{xy} indicates $MoGe_2$ is a multiband system. Herein, we fitted the Hall conductivity σ_{xy} and longitudinal conductivity σ_{xx} using a semiclassical two-band model:

$$\sigma_{xy} = \left(\frac{n_h\mu_h^2}{1 + (\mu_h B)^2} - \frac{n_e\mu_e^2}{1 + (\mu_e B)^2}\right)eB, \quad (4)$$

$$\sigma_{xx} = \frac{en_e\mu_e}{1 + (\mu_e B)^2} + \frac{\sigma_{xx}(0) - en_e\mu_e}{1 + (\mu_h B)^2}, \quad (5)$$

where n_h (n_e) and μ_h (μ_e) are the hole (electron) carrier density and hole (electron) mobility, respectively. We find that σ_{xy} and σ_{xx} can be well fitted from 2.5 K to 300 K using the two-band model, and typical fitting curves for T = 2.5 K are shown in the insets of Figs. 3(a) and 3(b), respectively. The temperature dependence of carriers densities and mobilities obtained by fitting σ_{xy} and σ_{xx} are depicted in Figs. 3(c)–3(f). One can see that the carrier densities and mobilities have similar temperature-dependent tendencies and the same order of magnitude, which indicates that the semiclassical two-band model has captured the main physics. At 2.5 K, $n_e = 2.67 \times 10^{20}\ cm^{-3}$, $n_h = 2.48 \times 10^{20}\ cm^{-3}$, $\mu_e = 1.2 \times 10^4\ cm^2\,(V\,s)^{-1}$, and $\mu_h = 0.95 \times 10^4\ cm^2\,(Vs)^{-1}$. The densities of holes and electrons, up to $10^{20}\ cm^{-3}$, are typical concentration of semimetals. The ratio $n_h/n_e = 0.93$ implies that the hole density is almost equal to the electron density at low temperatures, which indicates the balance between holes and electrons in the $MoGe_2$. Furthermore, the mobilities of holes and electrons reaches to $10^4\ cm^2\,(V\,s)^{-1}$, a relatively large order of magnitude, which reinforces the magnitude of the MR. The good agreement between the experimental result and the analysis of Hall resistivity ρ_{xy} and longitudinal conductivity σ_{xx} with the semiclassical two-band model confirms that the compensation of carriers and high mobilities at low temperatures are the origin of unsaturated quadratic LMR phenomenon and the upturn resistivity behavior in the $MoGe_2$. The consistency of two fitting results indicate the semiclassical two-band model is reliable to confirm the compensation of electrons and holes densities and to ensure the accuracy of the fitting results, which is commonly used in other TSMs, such as Ta_3S_2 [46]. As temperatures increase, the hole density keeps rising up, while the electron density is becoming smaller. Both hole mobility and electron mobility drop down with increasing temperatures. The abrupt changes for carriers densities and mobilities have also been observed in other TSMs, such as W_2As_3 [47], WTe_2 [48], and $ZrTe_5$ [49], in which the Lifshitz transition can induce the shift of Fermi level with temperature increasing, resulting in the loss of the electron-hole compensation.

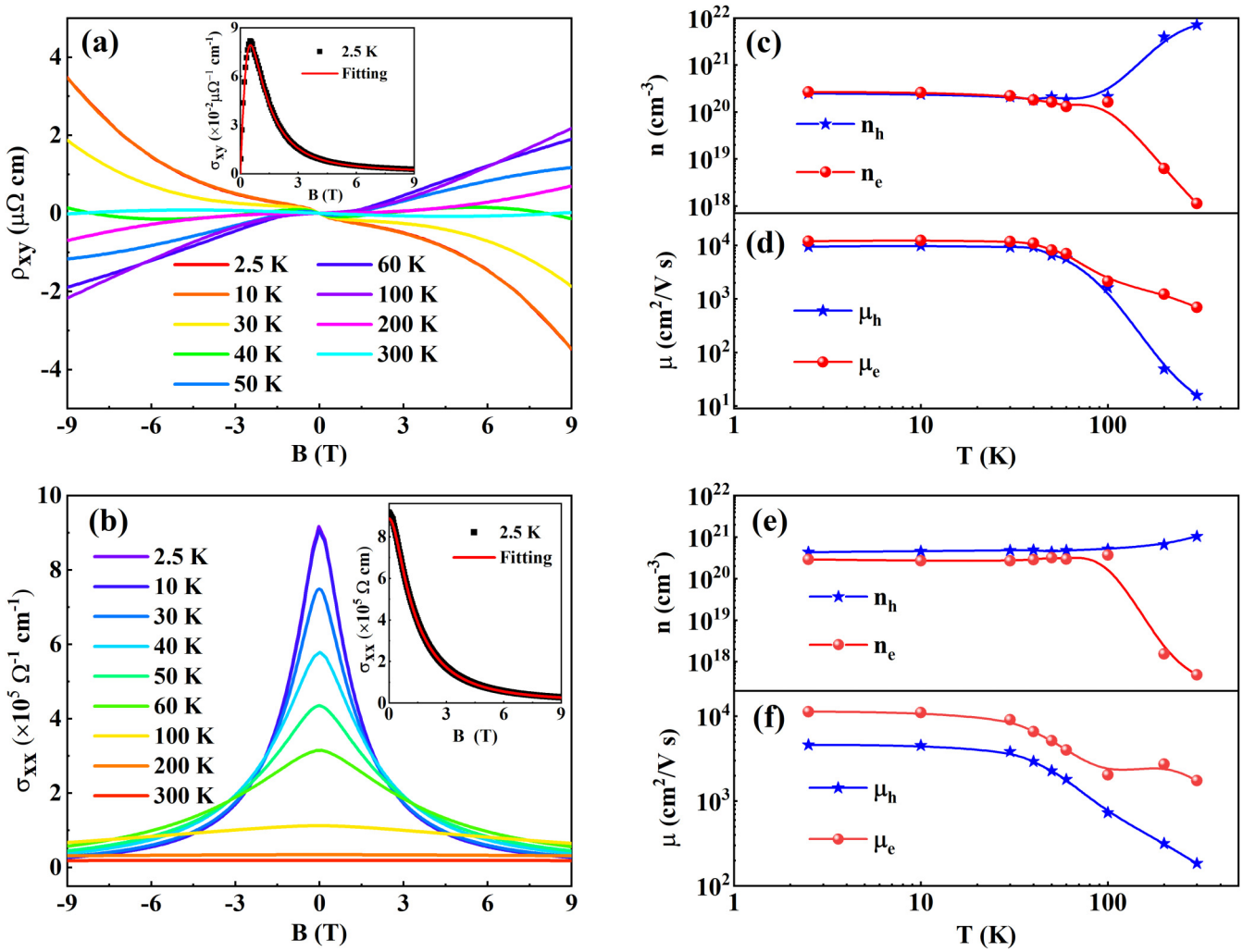

FIG. 3. (a) Magnetic field dependence of Hall resistivity ρ_{xy} at various temperatures. The inset presents the good fitting result at 2.5 K by semiclassical two-band model, where the black dots and red line are experimental data and fitting curve, respectively. (b) Magnetic field dependence of longitudinal conductivity σ_{xx} at different temperatures, inset of which is the good fitting result at 2.5 K by conductivity fitting formula. (c), (d), (e), and (f) show temperature dependence of carriers densities and mobilities of electrons and holes obtained by fitting Hall conductivity σ_{xy} and longitudinal conductivity σ_{xx}, respectively.

The isothermal magnetic field dependence of MR at 2.5 K with rotating B in the xz plane from $B \perp I$ ($\theta = 90°$) to $B \parallel I$ ($\theta = 0°$) is shown Fig. 4(a). We find that the MR has a maximum for $B \perp I$ ($\theta = 90°$) and considerably decreases with θ decreasing. When $B \perp I$ ($\theta = 0°$) at 2.5 K, as shown in Fig. 4(b), the MR presents two opposite regions, which reveals that there is a competition between two origins, one with positive response and the other with negative response to higher magnetic fields in the $MoGe_2$. At the weak-field regime (region I: $B \lesssim 1.4$ T), the positive response for MR can increase up to maximum 10% and a sharp MR dip is observed around zero field. This observation can be attributed to the WAL effect that has been commonly reported in TSMs, such as TaAs and $PtSe_2$ [12,50], in which Dirac fermions dominate the magnetoelectric transport process. While at higher-field regime (region II: $B \gtrsim 1.4$ T), the negative response for MR drops with oscillation-like behavior, which is due to measurement deviation, and reach a minimum of -30% without saturation at 9 T, similar to that reported in the TSM $TaSb_2$ [51]. Figure 4(c) shows that the WAL effect and longitudinal NMR are rapidly suppressed with temperatures increasing, and ultimately disappear until around 100 K. In addition, the longitudinal NMR, sensitive to the angle θ between magnetic fields and current, sharply decreases when θ is deviated from 0°, as presented in Fig. 4(d). Once θ is above 6°, the NMR becomes positive, which mainly results from components of positive LMR for $\theta = 90°$. In general, the NMR can be related to several mechanisms, including current jetting effect [52], weak localization (WL) effect [53,54], magnetic scattering [55,56], and ABJ chiral anomaly of Weyl nodes [12,36]. We consider here that ABJ anomaly is the most probable cause in the $MoGe_2$. Firstly, different from the temperature insensitivity of NMR in the current jetting effect, the NMR in the $MoGe_2$ is sensitive to temperature. Besides, current jetting effect is highly sensitive to the contact configuration. We have tried to use another contact configuration on the same sample and discovered the similar NMR phenomenon, which proves that current jetting effect may not play a leading

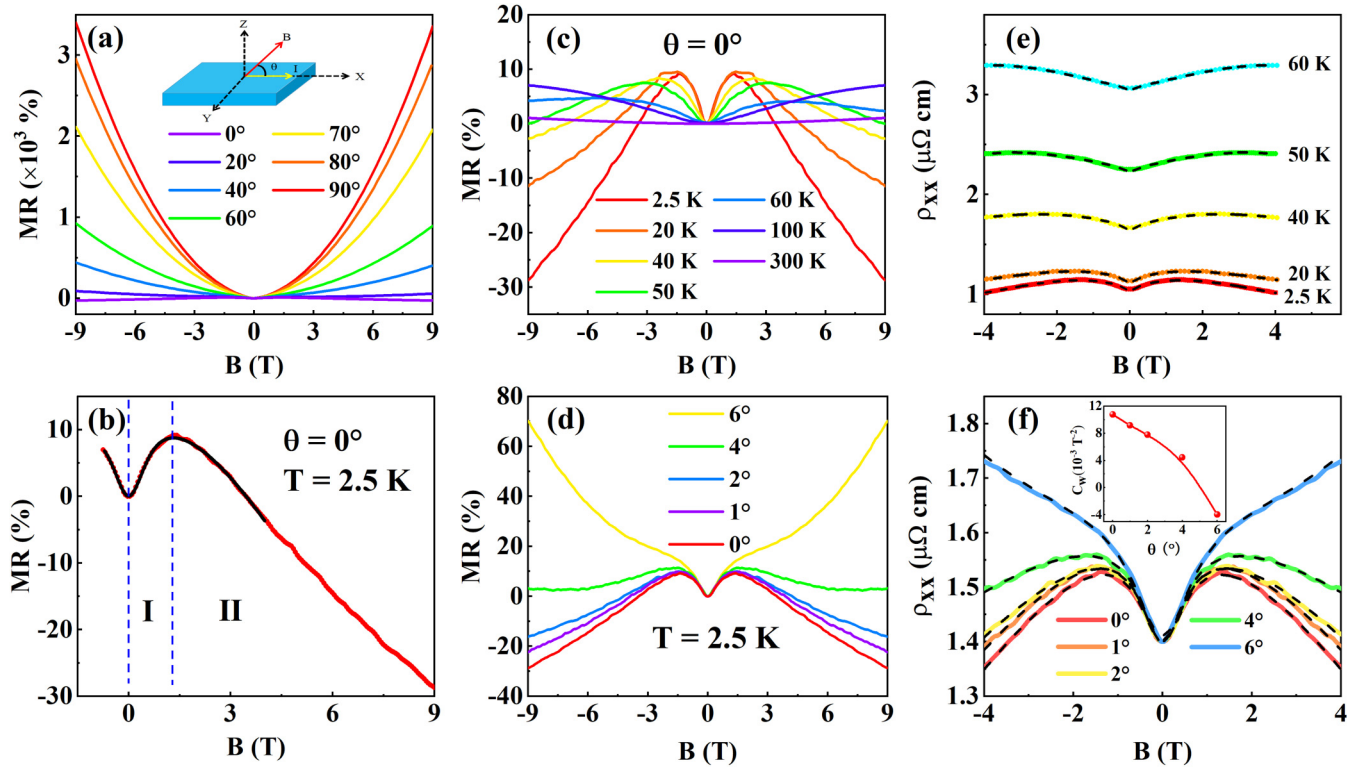

FIG. 4. (a) Magnetic field dependence of MR at 2.5 K with magnetic field varied from perpendicular to the current ($\theta = 90°$), to parallel to the current ($\theta = 0°$). (b) Magnetic field dependence of MR at 2.5 K with magnetic field parallel to the current, which can be divided into two regions, region I and region II. The solid curve is the ABJ theoretical fitting result. (c) Magnetic field dependence of MR at various temperatures for $\theta = 0°$. (d) Magnetic field dependence of MR at 2.5 K with θ close to $\theta = 0°$. (e) and (f) show the fitting curves of NMR at various temperatures and at different angles θ, respectively. The inset of (f) shows the strong angle θ sensitivity of C_W.

role in the NMR. Secondly, in regard to WL effect, strong NMR signal should be observed at $\theta = 90°$ and commonly exists at low-magnetic fields. However, unsaturated positive LMR is presented at $\theta = 90°$ and NMR can still exist at high-magnetic fields, which are inconsistent with WL effect evidently. Thirdly, because of the nonmagnetic nature of $MoGe_2$, magnetic scattering mechanism is naturally impossible to lead to NMR. Therefore, we hold that the longitudinal NMR of $MoGe_2$ is most likely attributed to ABJ anomaly in the presence of WAL corrections.

To further investigate the observed longitudinal NMR in the $MoGe_2$, we analyzed the NMR at different temperatures and different angles with magnetic field ranging from -4 T to 4 T using the semiclassical formula [12,36]:

$$\sigma(B) = (1 + C_W B^2)\sigma_{WAL} + \sigma_N, \tag{6}$$

$$\sigma_{WAL} = \sigma_0 + a\sqrt{B}, \tag{7}$$

$$\sigma_N{}^{-1} = \rho_0 + AB^2, \tag{8}$$

where C_W is a positive chiral coefficient originating from the topological term of $E \cdot B$. σ_{WAL} and σ_N are the conductivity from the contribution of quantum interference corrections associated with spin-orbit scattering and conventional bands other than topological-protected nodes, respectively. σ_0 and ρ_0 are the conductivity and resistivity, respectively, at zero field. Figures 4(e) and 4(f) show the experimental data (solid lines) and the fitting curves (black dashed lines) at various temperatures and different angles, respectively. We can see that the semiclassical magnetoconductance formula perfectly describes the MR data with magnetic field up to 4 T, which seems to suggest that $MoGe_2$ is of 3D Dirac or Weyl fermions' characters as observed in other TSMs [12,34,57]. What is more, the chiral anomaly coefficient C_W is strongly sensitive to the angle θ, as shown in the inset of Fig. 4(f), further confirming the presence of the ABJ chiral anomaly, which results in the observation of longitudinal NMR in the $MoGe_2$.

For a 3D topological material, the surface Dirac point can be separated into two Weyl nodes with opposite chirality in momentum space by breaking the spatial inversion symmetry or the time-reversal symmetry [12,57]. Herein, the emergence of longitudinal NMR observed in the $MoGe_2$ can be associated with the chiral anomaly of Weyl nodes, which may be split from the surface Dirac nodes with the application of high magnetic fields. Further band-structure calculations and experimental research are necessary to clarify this issue.

IV. SUMMARY

In summary, we have performed the magnetotransport measurements on the single crystal $MoGe_2$, which was proposed to be a new TI candidate. $MoGe_2$ exhibits a metallic behavior and an upturn resistivity behavior with magnetic fields ranging from 0 T to 9 T. Based on the semiclassical

two-band model, we find that $MoGe_2$ is an electron-hole compensation system with high mobilities, which is responsible for the unsaturated quadratic LMR and resistivity upturn at low temperatures. Remarkably, we observe the emergence of WAL effect at low fields, and a pronounced longitudinal NMR at higher fields, sensitive to temperatures and angles between B and E. By excluding other physical mechanisms, we speculate that the observed longitudinal NMR in the $MoGe_2$ is attributed to the ABJ chiral anomaly of Weyl nodes splitting from surface Dirac points. Our results clearly indicate that $MoGe_2$ is a typical TSM, rather than the theoretically predicated TI, which will encourage further theoretical and experimental investigations on this material.

ACKNOWLEDGMENTS

This work is supported by the National Key Research and Development Program of China (Grant No. 2016YFA0300604), the National Natural Science Foundation of China (Grant No. 11874417), and the Strategic Priority Research Program (B) of Chinese Academy of Sciences (Grant No. XDB33010100).

[1] M. Z. Hasan and C. L. Kane, Rev. Mod. Phys. **82**, 3045 (2010).
[2] X. L. Qi and S. C. Zhang, Rev. Mod. Phys. **83**, 1057 (2011).
[3] H. Zhang, C. Liu, X. Qi, X. Dai, Z. Fang, and S. Zhang, Nat. Phys. **5**, 438 (2009).
[4] Y. Chen *et al.*, Science **325**, 178 (2009).
[5] Z. Fang, N. Nagaosa, K. S. Takahashi, A. Asamitsu, R. Mathieu, T. Ogasawara, H. Yamada, M. Kawasaki, Y. Tokura, and K. Terakura, Science **302**, 92 (2003).
[6] S. Murakami, New J. Phys. **9**, 356 (2007).
[7] S. M. Young, S. Zaheer, J. C. Y. Teo, C. L. Kane, E. J. Mele, and A. M. Rappe, Phys. Rev. Lett. **108**, 140405 (2012).
[8] Z. Wang, Y. Sun, X.-Q. Chen, C. Franchini, G. Xu, H. Weng, X. Dai, and Z. Fang, Phys. Rev. B **85**, 195320 (2012).
[9] Z. Liu *et al.*, Nat. Mater. **13**, 677 (2014).
[10] J. Feng, Y. Pang, D. Wu, Z. Wang, H. Weng, J. Li, X. Dai, Z. Fang, Y. Shi, and L. Lu, Phys. Rev. B **92**, 081306(R) (2015).
[11] T. Liang, Q. Gibson, M. N. Ali, M. Liu, R. J. Cava, and N. P. Ong, Nat. Mater. **14**, 280 (2015).
[12] X. Huang *et al.*, Phys. Rev. X **5**, 031023 (2015).
[13] H. Weng, C. Fang, Z. Fang, B. A. Bernevig, and X. Dai, Phys. Rev. X **5**, 011029 (2015).
[14] B. Q. Lv *et al.*, Phys. Rev. X **5**, 031013 (2015).
[15] Z. Wang, D. Gresch, A. A. Soluyanov, W. Xie, S. Kushwaha, X. Dai, M. Troyer, R. J. Cava, and B. A. Bernevig, Phys. Rev. Lett. **117**, 056805 (2016).
[16] R. Yu, Z. Fang, X. Dai, and H. Weng, Front. Phys. **12**, 127202 (2017).
[17] J. Hu *et al.*, Phys. Rev. Lett. **117**, 016602 (2016).
[18] J. Ma *et al.*, Nat. Phys. **14**, 349 (2018).
[19] J. B. He, D. Chen, W. L. Zhu, S. Zhang, L. X. Zhao, Z. A. Ren, and G. F. Chen, Phys. Rev. B **95**, 195165 (2017).
[20] R. Lou *et al.*, Phys. Rev. B **96**, 241106(R) (2017).
[21] N. Kumar *et al.*, Nat. Commun. **8**, 1642 (2017).
[22] M. Matin, R. Mondal, N. Barman, A. Thamizhavel, and S. K. Dhar, Phys. Rev. B **97**, 205130 (2018).
[23] K. Deng *et al.*, Nat. Phys. **12**, 1105 (2016).
[24] S. Thirupathaiah *et al.*, Phys. Rev. B **95**, 241105(R) (2017).
[25] Y. Qi *et al.*, Nat. Commun. **7**, 11038 (2016).
[26] Y. Naidyuk *et al.*, 2D Mater. **5**, 045014 (2018).
[27] M. Vergniory, L. Elcoro, C. Felser, N. Regnault, B. A. Bernevig, and Z. Wang, Nature **566**, 480 (2019).
[28] F. Tang, H. C. Po, A. Vishwanath, and X. Wan, Nature **566**, 486 (2019).
[29] A. Brown, Nature **206**, 502 (1965).
[30] R. D. Ridder, G. V. Tendeloo, and S. Amelinckx, Phys. Status Solidi **33**, 383 (1976).
[31] R. J. Peavler and C. G. Beck Jr, J. Phys. Chem. **63**, 2058 (1959).
[32] V. M. Agoshkov, V. D. Gorbatenkov, S. V. Popova, and L. N. Fomicheva, J. Less-Common Met. **78**, 235 (1981).
[33] H.-J. Kim, K.-S. Kim, J.-F. Wang, M. Sasaki, N. Satoh, A. Ohnishi, M. Kitaura, M. Yang, and L. Li, Phys. Rev. Lett. **111**, 246603 (2013).
[34] N. P. Armitage, E. J. Mele, and A. Vishwanath, Rev. Mod. Phys. **90**, 015001 (2018).
[35] A. A. Zyuzin and A. A. Burkov, Phys. Rev. B **86**, 115133 (2012).
[36] J. Xiong, S. K. Kushwaha, T. Liang, J. W. Krizan, M. Hirschberger, W. Wang, R. J. Cava, and N. P. Ong, Science **350**, 413 (2015).
[37] F. Arnold *et al.*, Nat. Commun. **7**, 11615 (2016).
[38] H. Li, H. He, H.-Z. Lu, H. Zhang, H. Liu, R. Ma, Z. Fan, S.-Q. Shen, and J. Wang, Nat. Commun. **7**, 10301 (2016).
[39] J. Ziman, *Electrons and Phonons* (Oxford University Press, Oxford, 1960), Vol. 14.
[40] S. Sun, Q. Wang, P.-J. Guo, K. Liu, and H. Lei, New J. Phys. **18**, 082002 (2016).
[41] L.-L. Sun, Y.-Y. Wang, S. Xu, and T.-L. Xia, Europhys. Lett. **120**, 37002 (2018).
[42] Z. Yuan, H. Lu, Y. Liu, J. Wang, and S. Jia, Phys. Rev. B **93**, 184405 (2016).
[43] Y.-Y. Wang, Q.-H. Yu, P.-J. Guo, K. Liu, and T.-L. Xia, Phys. Rev. B **94**, 041103(R) (2016).
[44] Y. L. Wang *et al.*, Phys. Rev. B **92**, 180402(R) (2015).
[45] P.-J. Guo, H.-C. Yang, B.-J. Zhang, K. Liu, and Z.-Y. Lu, Phys. Rev. B **93**, 235142 (2016).
[46] D. Chen *et al.*, Phys. Rev. B **94**, 174411 (2016).
[47] Y. Li, C. Xu, M. Shen, J. Wang, X. Yang, X. Yang, Z. Zhu, C. Cao, and Z.-A. Xu, Phys. Rev. B **98**, 115145 (2018).
[48] Y. Wu, N. H. Jo, M. Ochi, L. Huang, D. Mou, S. L. Bud'ko, P. C. Canfield, N. Trivedi, R. Arita, and A. Kaminski, Phys. Rev. Lett. **115**, 166602 (2015).
[49] Y. Zhang *et al.*, Nat. Commun. **8**, 15512 (2017).
[50] Z. Li, Y. Zeng, J. Zhang, M. Zhou, and W. Wu, Phys. Rev. B **98**, 165441 (2018).
[51] Y. Li, L. Li, J. Wang, T. Wang, X. Xu, C. Xi, C. Cao, and J. Dai, Phys. Rev. B **94**, 121115(R) (2016).

[52] J. Hu, T. F. Rosenbaum, and J. B. Betts, Phys. Rev. Lett. **95**, 186603 (2005).
[53] Y. Wang and J. J. Santiago-Avilés, J. Appl. Phys. **94**, 1721 (2003).
[54] S. Kawaji, Surf. Sci. **170**, 682 (1986).
[55] S. Von Molnar and S. Methfessel, J. Appl. Phys. **38**, 959 (1967).
[56] H. Chiba, M. Kikuchi, K. Kusaba, Y. Muraoka, and Y. Syono, Solid State Commun. **99**, 499 (1996).
[57] D. Sinha and G. A. J. Amaratunga, Phys. Rev. Lett. **114**, 147701 (2015).